

Article

Low-Temperature Selective NO Reduction by CO over Copper-Manganese Oxide Spinel

Fenglan Fan ¹, Lingjuan Wang ¹, Lei Wang ¹, Jinyu Liu ^{1,*}  and Minghui Wang ^{2,*}

¹ School of Chemistry and Chemical Engineering, Hebei Normal University for Nationalities, Chengde 067000, China; ffl619@163.com (F.F.); lingjuan1992@163.com (L.W.); lanlan19870619@163.com (L.W.)

² School of Chemical Engineering, Changchun University of Technology, Changchun 130012, China

* Correspondence: llhliulu@163.com (J.L.); whm0932@ccut.edu.cn (M.W.)

Abstract: Selective catalytic reduction of NO with CO (CO-SCR) has been suggested as an attractive and promising technology for removing NO and CO simultaneously from flue gas. Manganese-copper spinels are a promising CO-SCR material because of the high stability and redox properties of the spinel structure. Here, we synthesized $\text{Cu}_x\text{Mn}_{3-x}\text{O}_4$ spinel by a citrate-based modified pechini method combining CuO and MnO_x , controlling the molar Cu/Mn concentrations. All the samples were characterized by SEM, EDX, XRD, TEM, H_2 -TPR, XPS and nitrogen adsorption measurements. The $\text{Cu}_{1.5}\text{Mn}_{1.5}\text{O}_4$ catalyst exhibits 100% NO conversion and 53.3% CO conversion at 200 °C. The $\text{Cu}_x\text{Mn}_{3-x}\text{O}_4$ catalyst with Cu-O-Mn structure has a high content of high valence Mn, and the high mass transfer characteristics of the foam-like structure together promoted the reaction performance. The CO-SCR catalytic performance of Cu was related to the spinel structure with the high ratio of Mn^{4+}/Mn , the synergistic effect between the two kinds of metal oxides and the multistage porous structure.

Keywords: low-temperature; CO-SCR; Cu-Mn oxide spinels



Citation: Fan, F.; Wang, L.; Wang, L.; Liu, J.; Wang, M. Low-Temperature Selective NO Reduction by CO over Copper-Manganese Oxide Spinel. *Catalysts* **2022**, *12*, 591. <https://doi.org/10.3390/catal12060591>

Academic Editor: Sónia Carabineiro

Received: 22 April 2022

Accepted: 27 May 2022

Published: 29 May 2022

Publisher's Note: MDPI stays neutral with regard to jurisdictional claims in published maps and institutional affiliations.



Copyright: © 2022 by the authors. Licensee MDPI, Basel, Switzerland. This article is an open access article distributed under the terms and conditions of the Creative Commons Attribution (CC BY) license (<https://creativecommons.org/licenses/by/4.0/>).

1. Introduction

Currently, environmental protection is more stringent than ever before. The large quantities of nitrogen oxides (NO_x) produced by the burning of fossil fuels are a major cause of atmospheric pollutants. Carbon monoxide (CO) is another atmospheric pollutant in flue gases. Thus, the reduction of NO by the CO produced by incomplete combustion in the flue gas can remove toxic CO and NO simultaneously and economically (CO-SCR) [1–3]. However, the high price and low catalytic activity at low temperature (more than 50% NO conversion below 250 °C) of efficient noble metal catalysts seriously limit their further application. Therefore, it is necessary to develop catalysts with low temperature, high performance, low cost and that are green [4].

For the CO-SCR reaction, the ideal catalyst should not only be economical, easy to prepare, long-term stable and so on. In addition, a low reaction temperature [5,6], high selectivity [7,8] and NO conversion rate [9] are required. Noble metals are frequently used in CO-SCR reactions to prepare noble-metal catalysts. However, the scarce resources, high price and high temperature instability limit its large-scale application. As a result, many studies have focused on the development of nonprecious metals. NO reduction occurs through a redox reaction mechanism. Therefore, the reducibility and oxygen migration ability of the catalyst are two key factors that determine the catalytic performance of the catalyst for NO removal. At present, metal oxides have become a hotspot of heterogeneous catalysis research because of their low price and large reserves, such as CoO_x [10,11], CuO_x [12–14], MnO_x [15,16] and CeO_2 [17]. Among them, copper oxides and manganese oxides have attracted much attention due to their good redox properties. Manganese oxides show a variety of valences (Mn^{2+} , Mn^{3+} , Mn^{4+}) and abundant reactive oxygen species

(vacancy oxygen and adsorbed oxygen), which imply their potential in low-temperature CO-SCR catalysis [18–20].

In related reports, the reducibility and oxygen migration ability of MnO_x could be improved by proper cation doping. These include MnCe [21], MnCu [22–24], MnCo [25], MnNi [26,27] and MnFe [28]. Because of its excellent oxidation–reduction performance and strong synergistic effect between binary metal oxides, doping copper into the catalyst can effectively improve the removal rate of the catalyst. Wan et al. [29] found that the Mn_2O_3 -modified $\text{CuO}/\gamma\text{-Al}_2\text{O}_3$ catalyst showed significant catalytic efficiency, and they attributed the increase in activity to the establishment of a $\text{Cu}^{2+} + \text{Mn}^{3+} \rightleftharpoons \text{Cu}^+ + \text{Mn}^{4+}$ oxidation–reduction cycle. In addition, the addition of Cu to Mn-based catalysts is beneficial to the dispersion of MnO_x . The performance of copper oxides is affected by many factors in the NO + CO reaction. Ivanka Spassova [24] reported that CuCo_2O_4 and $\text{Cu}_{1.5}\text{Mn}_{1.5}\text{O}_4$ mixed oxides supported on DFS were responsible for enhancing activity. The results showed that Liu [30] suggested that copper-modified manganites had higher catalytic activity for CO oxidation and selective catalytic reduction of NO than pure MnO_x . Therefore, it is further expected that CuO and MnO_x form a strong coupling at the nanointerface, which will lead to a change in the Mn^{4+} octahedral environment, thereby further improving the CO–SCR performance of MnO_x .

This article reports that foam-like $\text{Cu}_x\text{Mn}_{3-x}\text{O}_4$ spinels were prepared by using a citrate-based modified pechini method and applied to the CO-SCR reaction in the temperature range of 100–400 °C. It was characterized by scanning electron microscopy (SEM), transmission electron microscopy (TEM), X-ray diffraction (XRD), BET surface area (BET), H_2 temperature programmed reduction (H_2 –TPR) and X-ray photoelectron spectroscopy (XPS). The structure–activity relationship between the physical chemistry properties and the catalytic performance of the $\text{Cu}_x\text{Mn}_{3-x}\text{O}_4$ catalyst with different concentrations of Mn^{4+} was studied. The purpose of this work is to investigate the relationship between the active phase of spinel and the bulk properties of $\text{Cu}_x\text{Mn}_{3-x}\text{O}_4$ ($x = 0, 1, 1.5, 2, 3$) catalysts prepared with different CuO/ MnO_x contents.

2. Results and Discussion

2.1. XRD Analysis of Catalysts

XRD patterns were tested to identify the crystal structure of Mn_2O_3 , CuO and synthesized $\text{Cu}_x\text{Mn}_{3-x}\text{O}_4$ spinels. As shown in Figure 1a, for the Mn_2O_3 sample, (200), (211), (222), (123), and (440) planes of Mn_2O_3 (JCPDS#01-076-0150) could be observed at 18.5°, 23.1°, 33.0°, 35.7° and 55.0°, respectively. The diffraction peaks of 32.5°, 35.5°, 38.6°, 48.9°, 53.4°, 58.2°, 61.5°, 66.3°, 67.7°, 68.0°, 72.3° and 82.6° were assigned to the (110), (−111), (111), (−202), (020), (202), (−113), (−311), (113), (220), (311) and (−313) planes of cubic phase CuO (JCPDS#01-080-0076). A $\text{Cu}_x\text{Mn}_{3-x}\text{O}_4$ mixed oxide with a spinel structure was found in the $\text{Cu}_1\text{Mn}_2\text{O}_4$ (JCPDS#01-074-2422), $\text{Cu}_{1.5}\text{Mn}_{1.5}\text{O}_4$ (JCPDS#01-070-0260) and $\text{Cu}_2\text{Mn}_1\text{O}_4$ catalysts. XRD patterns show that the diffraction peak (I peak) can match spinel $\text{Cu}_{1.5}\text{Mn}_{1.5}\text{O}_4$ (Figure 1b). Compared with other samples, the intensity of the “I” diffraction peak of the $\text{Cu}_{1.5}\text{Mn}_{1.5}\text{O}_4$ sample is the strongest, indicating that the $\text{Cu}_{1.5}\text{Mn}_{1.5}\text{O}_4$ sample contains a spinel active structure (Cu–O–Mn) [30,31]. As for $\text{Cu}_1\text{Mn}_2\text{O}_4$ and $\text{Cu}_{1.5}\text{Mn}_{1.5}\text{O}_4$, they showed identical diffraction patterns to Mn_2O_3 but only with a slight shift in the peak position of Mn_2O_3 toward high values, implying the insertion of Cu atoms with smaller radius than Mn atoms into the lattice of Mn_2O_3 . It is also noticed that the crystallinity of $\text{Cu}_{1.5}\text{Mn}_{1.5}\text{O}_4$ becomes higher in comparison with that of $\text{Cu}_1\text{Mn}_2\text{O}_4$ and $\text{Cu}_2\text{Mn}_1\text{O}_4$, implying that excessive Cu doping is not conducive to the formation of Cu–O–Mn structure (Table 1). The lattice parameters of the synthesized $\text{Cu}_x\text{Mn}_{3-x}\text{O}_4$ catalyst were calculated by XRD, as shown in Table 1. Compared to $\text{Cu}_x\text{Mn}_{3-x}\text{O}_4$ spinels, the lattice parameters of $\text{Cu}_x\text{Mn}_{3-x}\text{O}_4$ spinels became smaller after doping with increased copper contents. The results also prove the above conclusions.

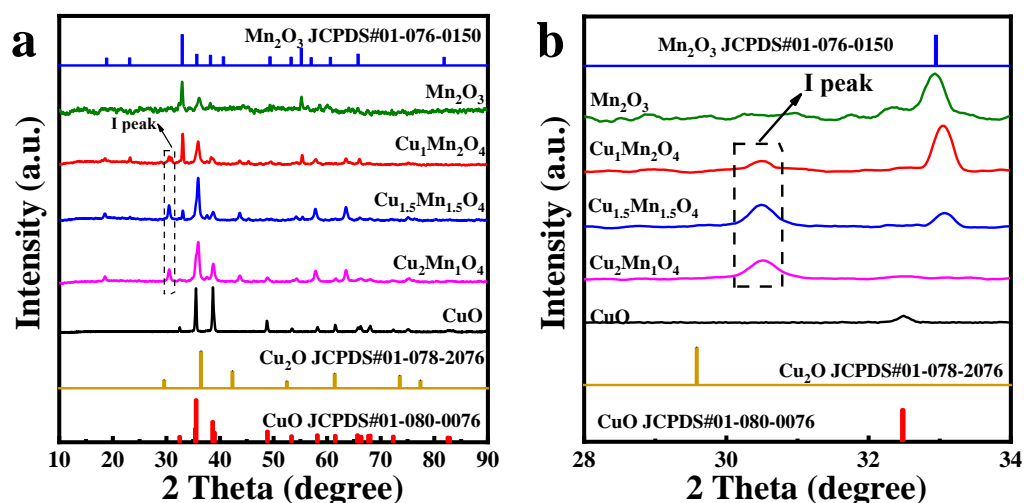


Figure 1. XRD patterns (a), local enlargement of (I) in XRD (b) of the as-synthesized $\text{Cu}_x\text{Mn}_{3-x}\text{O}_4$ samples.

Table 1. Crystal sizes, lattice parameters, actual molar ratios of Cu to Mn and BET surface areas of $\text{Cu}_x\text{Mn}_{3-x}\text{O}_4$.

Sample	Crystal Size nm	Lattice Parameter ^a nm	Actual Molar Ratios of Cu:Mn ^b	BET Surface Area $\text{m}^2 \text{g}^{-1}$ ^c
Mn_2O_3	63.07	$a = b = c = 0.9423$	-	18.2
$\text{Cu}_1\text{Mn}_2\text{O}_4$	42.69	$a = b = c = 0.8290$	0.93:2.05	18.9
$\text{Cu}_{1.5}\text{Mn}_{1.5}\text{O}_4$	31.79	$a = b = c = 0.8284$	1.46:1.54	19.7
$\text{Cu}_2\text{Mn}_1\text{O}_4$	31.76	$a = b = c = 0.8282$	1.97:1.02	18.7
CuO	42.43	$a = 0.4687, b = 0.3427,$ $c = 0.5135$	-	28.9

^a Calculated $2\theta = 33.0^\circ$ by the XRD patterns using the Debye–Scherrer equation. ^b Obtained by the ICP results. ^c Surface area derived from the BET equation.

2.2. N_2 Sorption Analysis of Catalysts

Figure 2 illustrates the obtained N_2 adsorption-desorption isotherm and pore size distribution of all the catalysts. The $\text{Cu}_x\text{Mn}_{3-x}\text{O}_4$ samples have type IV isotherms, which also proves that the samples possess a mesopores and significant macropores structure, and that the results of mesopores or macroporous foamy network structure are consistent with that of SEM. The low-pressure part of the near-linear middle part of the isotherm curve can be attributed to the unsaturated adsorption of single or multilayers, which also proves the existence of a macroporous structure. However, the hysteresis loops in the high p/p_0 range are related to capillary condensation in the mesopores, indicating that there are mesopores on the wall of the macropores. In addition, the corresponding Barrett–Joyner–Halenda (BJH) pore-size distribution curves in Figure 2b show that the $\text{Cu}_x\text{Mn}_{3-x}\text{O}_4$ samples have mesoporous and macroporous structures with a large distribution range of pore [32]. It should be pointed out that of the $\text{Cu}_{1.5}\text{Mn}_{1.5}\text{O}_4$ catalyst own the largest BET surface area and most mesoporous among the $\text{Cu}_x\text{Mn}_{3-x}\text{O}_4$ catalysts, Cu doping leads to the formation of more $\text{Cu}_{1.5}\text{Mn}_{1.5}\text{O}_4$ spinel structures, resulting in irregular changes in grain size. The specific surface areas of Cu–Mn spinel oxides with different Cu/Mn ratios are recorded in Table 1. The corresponding results conform to the XRD analysis of the catalysts.

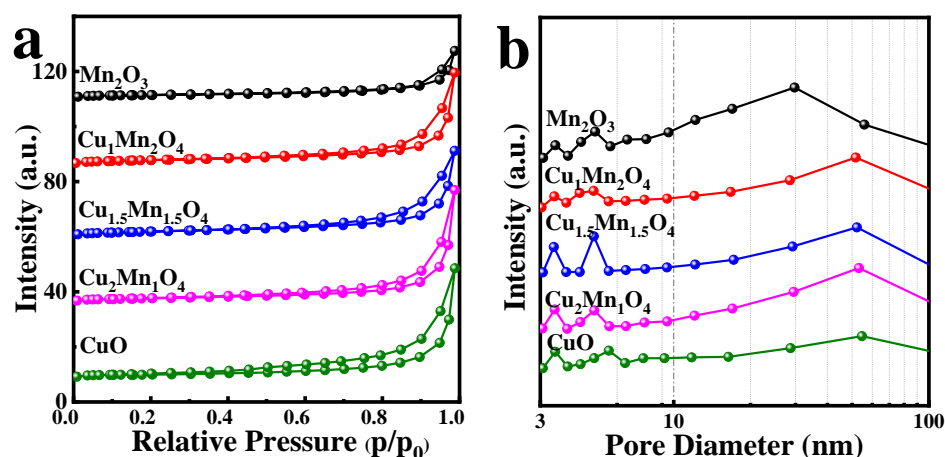


Figure 2. N_2 adsorption-desorption isotherms (a) and pore size distributions (b) of the as-synthesized $Cu_xMn_{3-x}O_4$ samples.

2.3. SEM and TEM Observation

The morphology and structural characteristics of the as-prepared catalysts at different molar ratios of Cu/Mn were characterized, as shown in Figure 3. Figure 3a,b show SEM images of pure Mn_2O_3 at different magnifications. The Mn_2O_3 sample is mainly composed of a foam structure with a diameter of 5–20 μm . The magnified SEM image further revealed that the surface of these particles had a hierarchical porous structure. In addition, with increasing Cu doping content, the surface of $Cu_xMn_{3-x}O_4$ catalyst particles becomes irregular, and the foam-like particles are broken into a uniform particle structure with a smaller particle size in Figure 3c–j. The mapping of $Cu_xMn_{3-x}O_4$ sample images is displayed in Figure 3k₁–k₄. It can be clearly observed that copper and manganese elements are uniformly dispersed on the entire catalyst surface.

Figure 4 shows the morphologies and microstructures of the $Cu_{1.5}Mn_{1.5}O_4$ catalyst at different magnifications. Combined with the SEM results, spherical nanoparticles with particle sizes ranging from 20 to 40 nm were formed in the $Cu_{1.5}Mn_{1.5}O_4$ sample. According to the equipped $Cu_{1.5}Mn_{1.5}O_4$ standard card (JCPDS#01-070-0260), the 0.48 and 0.25 nm lattice fringes can be matched to the (111) and (311) crystal planes of the $Cu_{1.5}Mn_{1.5}O_4$ spinel structure, respectively. It is worth noting that there was a strong synergistic interaction between Cu and Mn oxides in the active components of the spinel structure. Compared with $Cu_2Mn_1O_4$ spinel, $Cu_{1.5}Mn_{1.5}O_4$ has low crystallinity and can provide more oxygen vacancies, which may improve the catalytic performance of Cu-Mn catalysts in CO-SCR [30].

2.4. H_2 -TPR Analysis

The H_2 -TPR data of $Cu_xMn_{3-x}O_4$ samples are exhibited in Figure 5. Four peaks were observed on the Mn_2O_3 sample at 385, 466, 524 and 651 $^{\circ}C$, respectively. The relatively weak reduction peak at low temperature is due to the existence of surface species that can be easily reduced, that is, Mn_2O_3 is reduced to Mn_3O_4 . The strong reduction peak at high temperature can be attributed to the reduction of Mn_3O_4 to MnO , which is attributed to the manganese in the spinel phase. Mn_3O_4 is generally considered to consist of Mn^{2+} and Mn^{3+} . However, Mn^{4+} appears in the samples due to the equilibrium state of $2Mn^{3+} \rightleftharpoons Mn^{4+} + Mn^{2+}$. This phenomenon shows that the valence state of the Mn cation was complex in the Mn_3O_4 spinel, which may be of significance and be responsible for the completion of the catalytic cycle. For the $Cu_1Mn_2O_4$ spinel in Figure 5, there are only two well-defined reduction peaks at 298 and 351 $^{\circ}C$. The first reduction peak at 298 $^{\circ}C$ was attributed to the reduction of Cu^{2+} to Cu^+ , and the second reduction peak at 351 $^{\circ}C$ corresponded to the three reduction processes: the reduction of $Mn^{4+} \rightarrow Mn^{3+}$, $Mn^{3+} \rightarrow Mn^{2+}$ and $Cu^+ \rightarrow Cu^0$. The changes in the reduction peak number, reduction temperature and

peak intensity showed that there is electron transfer between Cu ions and Mn ions in the spinel lattice ($\text{Mn}^{3+} + \text{Cu}^{2+} \rightleftharpoons \text{Mn}^{4+} + \text{Cu}^+$), and the presence of the strong interaction between Cu and Mn could play a synergistic role in the reducibility of the catalysts, leading to the enhancement of the catalytic cycle in CO-SCR [29].

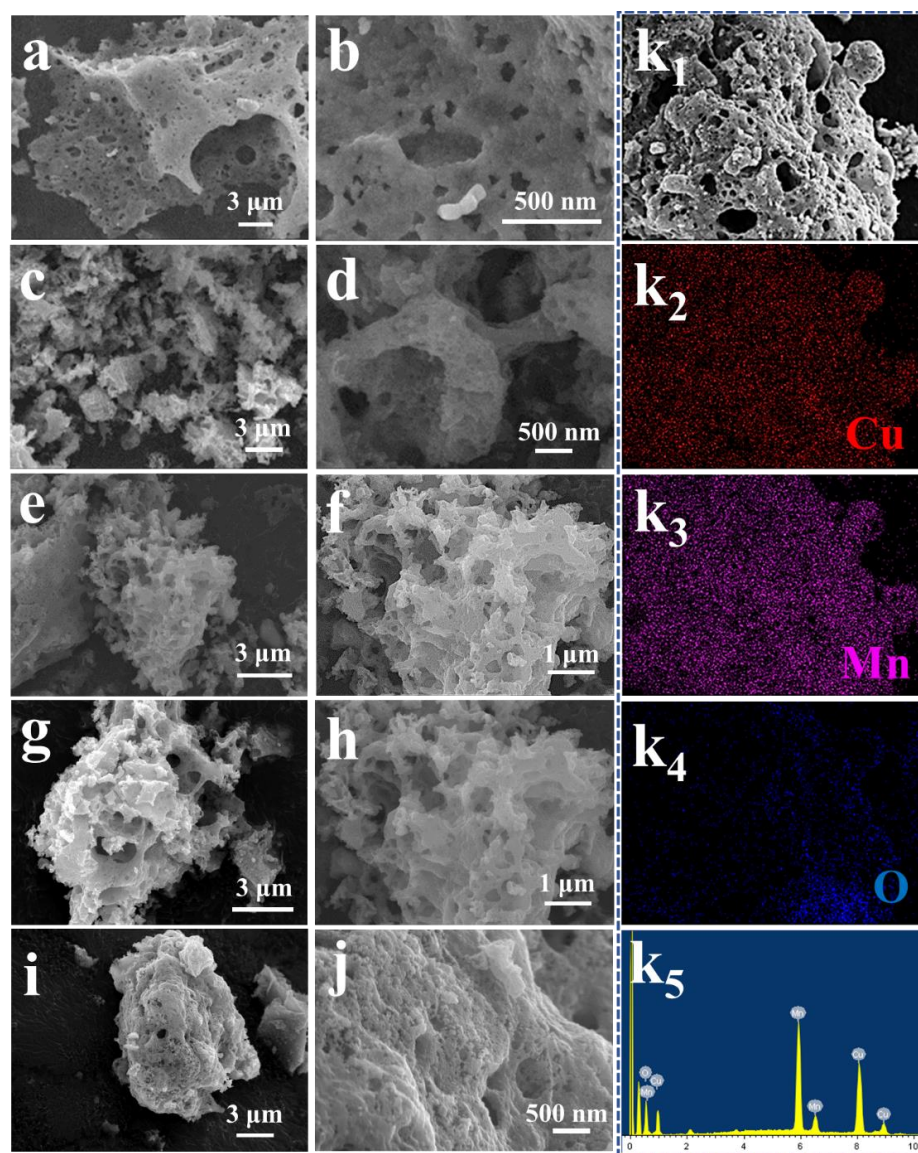


Figure 3. SEM images of Mn_2O_3 (a,b), $\text{Cu}_1\text{Mn}_2\text{O}_4$ (c,d), $\text{Cu}_{1.5}\text{Mn}_{1.5}\text{O}_4$ (e,f), $\text{Cu}_2\text{Mn}_1\text{O}_4$ (g,h) and CuO (i,j). Cu, Mn and O elemental mapping recordings from $\text{Cu}_{1.5}\text{Mn}_{1.5}\text{O}_4$ (k_1 – k_4) and the EDS result (k_5).

For the $\text{Cu}_{1.5}\text{Mn}_{1.5}\text{O}_4$ sample, the low-temperature reduction peak reaches the same temperature (298°C), and the high-temperature reduction peak moves to a lower temperature (342°C). This phenomenon can be explained by the reduction in lattice distortion and the strong interaction between copper and manganese. Compared with $\text{Cu}_2\text{Mn}_1\text{O}_4$, the two reduction peaks of $\text{Cu}_2\text{Mn}_1\text{O}_4$ (at 299 and 328°C) have shifted to lower values. It is noteworthy that as the Cu doping content increased, the low-temperature reduction peaks of all catalysts became stronger. These results indicate that the interaction between Cu and Mn is enhanced, and that the redox property is improved with an increasing Cu doping amount.

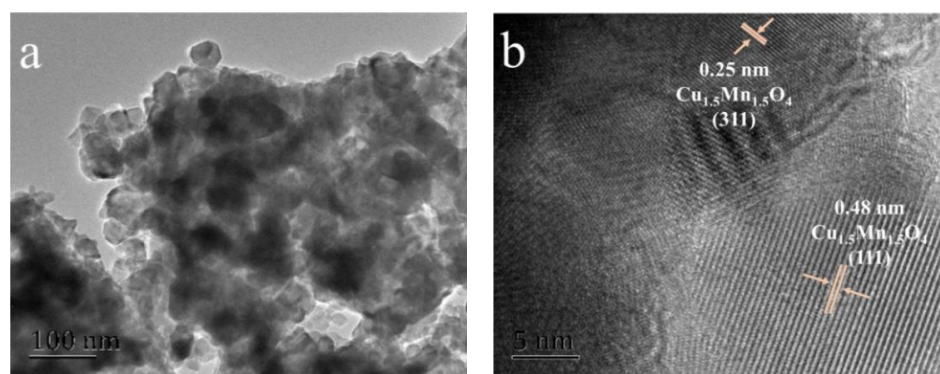


Figure 4. TEM image (a) and HRTEM image (b) of the $\text{Cu}_{1.5}\text{Mn}_{1.5}\text{O}_4$ sample.

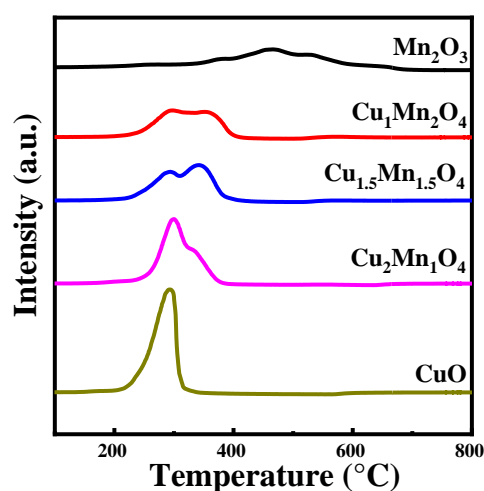


Figure 5. H_2 -TPR curves of the as-synthesized $\text{Cu}_x\text{Mn}_{3-x}\text{O}_4$ samples.

2.5. XPS Analysis

XPS was obtained on the $\text{Cu}_x\text{Mn}_{3-x}\text{O}_4$ sample, and the spectra of Cu 2p, Mn 2p and O 1s scans, as well as C from the reference, are shown in Figure 6a. The Cu 2p 3/2 spectra could be divided into two characteristic peaks attributed to Cu^+ (931.0 eV) and Cu^{2+} (934.1 eV) by performing peak-fitting deconvolutions, we can also see that accompanied by two distinct satellite peaks (marked by Sat.) at 938.2–945.9 and 959.7–964.7 eV in Figure 6b, which confirms the presence of Cu^{2+} . The content of $\text{Cu}^{+/0}$ of $\text{Cu}_{1.5}\text{Mn}_{1.5}\text{O}_4$ is the highest among the $\text{Cu}_x\text{Mn}_{3-x}\text{O}_4$. This result validated the existence of electron transfer between Cu ions and Mn ions ($\text{Mn}^{3+} + \text{Cu}^{2+} \rightleftharpoons \text{Mn}^{4+} + \text{Cu}^+$) in the $\text{Cu}_{1.5}\text{Mn}_{1.5}\text{O}_4$ spinel (Table 2). The spectra recorded from the $\text{Cu}_{1.5}\text{Mn}_{1.5}\text{O}_4$ sample consist of a broad spin-orbit double peak, indicating the presence of more than one Mn contribution. An obvious feature of this spectrum is that the high binding energy side of the main peaks 2p3/2 and 2p1/2 are obviously the Mn 2p3/2 spectra, and could be divided into three characteristic peaks attributed to Mn^{2+} (640.7 eV), Mn^{3+} (641.8 eV), and Mn^{4+} (643.9 eV), respectively (Figure 6c). The results show that the $\text{Cu}_{1.5}\text{Mn}_{1.5}\text{O}_4$ sample contains the highest content of Mn^{4+} ions (54.4%), which indicates that Cu replaces the low valence Mn cations and significantly promotes the formation of high valence Mn cations. This result support the TPR results. In other words, due to the strong interaction between manganese and copper oxide (Cu), there are some electronic interactions between Mn^{4+} and Cu^+ (Cu–O–Mn bridge). To study the different O species on the surface of the $\text{Cu}_x\text{Mn}_{3-x}\text{O}_4$ samples, the O 1s photoelectron spectra were obtained, as shown in Figure 6d. The deconvoluted peaks indicate that there are two different kinds of O species on the surface of the catalyst. The split peak at a lower binding energy of approximately 531.4 eV corresponds to lattice oxygen (denoted as O_α), and the other peak at approximately 529.5 eV is assigned to surface chemisorbed oxygen,

potentially including the chemisorbed oxygen O_2^{2-} or defective O^- (denoted as O_β). The doping of Cu leads to the partial substitution of Cu atoms for Mn atoms in the $-O-Mn-$ structure ($O-Cu$), which enhances the instability of O species and forms more active O species. This result is similar to the conclusion in the reported literature [30].

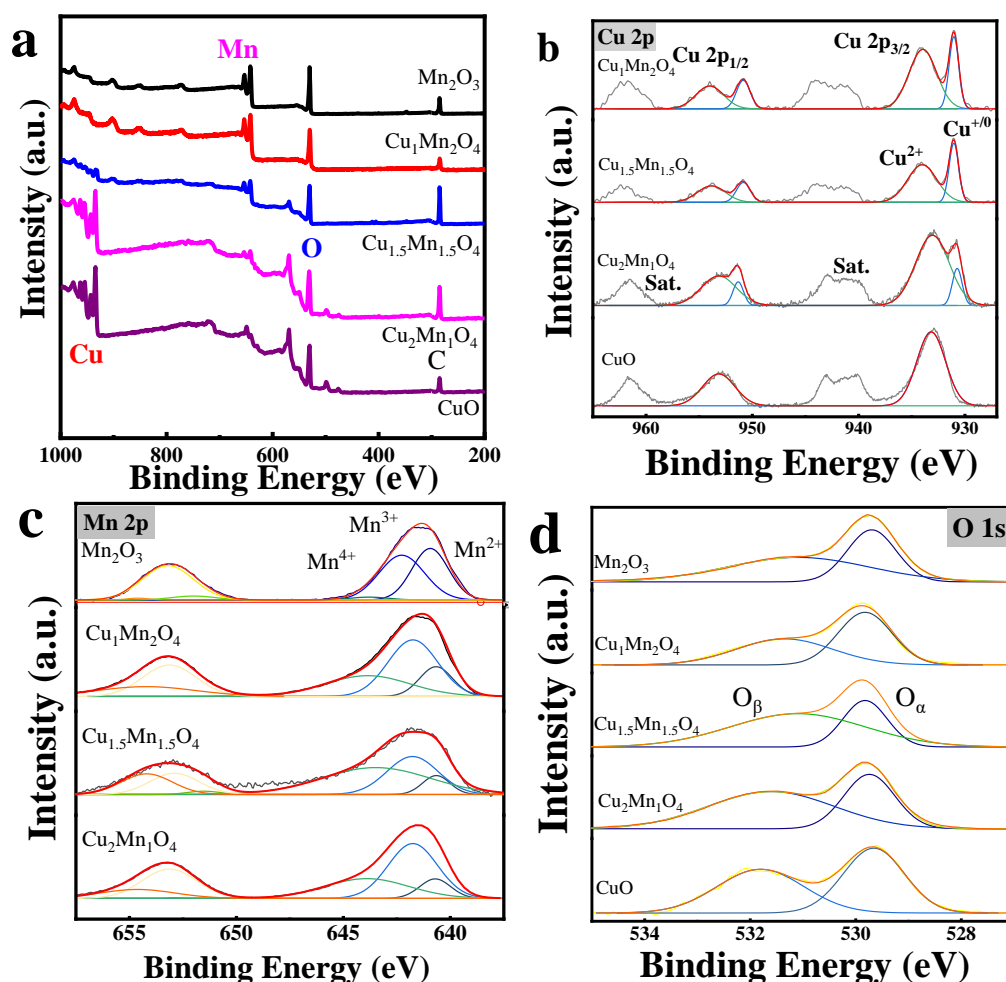


Figure 6. Survey spectra (a), Cu 2p (b), Mn 2p (c) and O 1s, (d) XPS spectra of $Cu_xMn_{3-x}O_4$ catalysts.

Table 2. XPS results of all the catalysts.

Sample	Mn ⁴⁺ /Mn	Mn ³⁺ /Mn	Mn ²⁺ /Mn	Cu ²⁺ /Cu	O _α /O	O _β /O
Mn ₂ O ₃	2.7	50.7	46.6	-	55.4	44.6
Cu ₁ Mn ₂ O ₄	31.6	50.8	17.6	70.1	53.1	46.9
Cu _{1.5} Mn _{1.5} O ₄	54.4	36.0	9.6	66.2	32.3	67.7
Cu ₂ Mn ₁ O ₄	33.4	54.4	12.2	86.7	37.5	62.5
CuO	-	-	-	100	51.1	48.9

3. Catalytic Performances of the Catalysts

3.1. Catalytic Reduction of NO with CO

In the temperature range 100–400 °C, the catalytic performance of the synthesized materials for the reduction of NO by CO is shown in Figure 7. It can be seen that pure Mn₂O₃ has CO-SCR catalytic activity, the NO conversion rate can reach 100% at a temperature of approximately 350 °C, and the CO conversion rate is the worst. It can be clearly found that the catalytic activity of all Cu-doped catalysts is significantly higher than that of manganese oxide catalysts in the test temperature range. The CO-SCR activities of the Cu_{1.5}Mn_{1.5}O₄ catalyst exhibited the best NO conversion when the temperature was below

200 °C. High-valence state spinel is the active component of the CO-SCR reaction, which is more conducive to showing better low-temperature activity, as reported in the literature. The CO conversion of the Cu-doped catalyst has a similar trend with the increase of temperature, and the CO conversion data are inconsistent with the NO conversion data above 200 °C, implying that CO reduced partial metal oxides in Figures 7c and S1 (consistent with the H₂-TPR result). From the CO catalytic activity results, it can be seen that the Cu-doped catalyst shows better catalytic activity than the pure Mn₂O₃ sample. The Cu₂Mn₁O₄ sample shows a higher CO catalytic oxidation activity, which suggests that excessive copper doping causes the adsorption of CO to be stronger than that of NO. This also implies that the Cu–O–Mn structure in spinel is the active site of CO-SCR (corresponding to the XRD results). The reaction of CO-SCR under O₂-rich conditions was performed to investigate the effect of O₂ on the catalytic performance. As shown in Figure S2, the NO conversion of the catalyst significantly decreased, and CO conversion increased with the increase of temperature. It can be found that the main reason affecting the NO conversion is the competitive reaction between CO and NO with O₂, resulting in the decline of performance. Improving the low-temperature catalytic performance of the catalyst under oxygen conditions will be the focus of our future research.

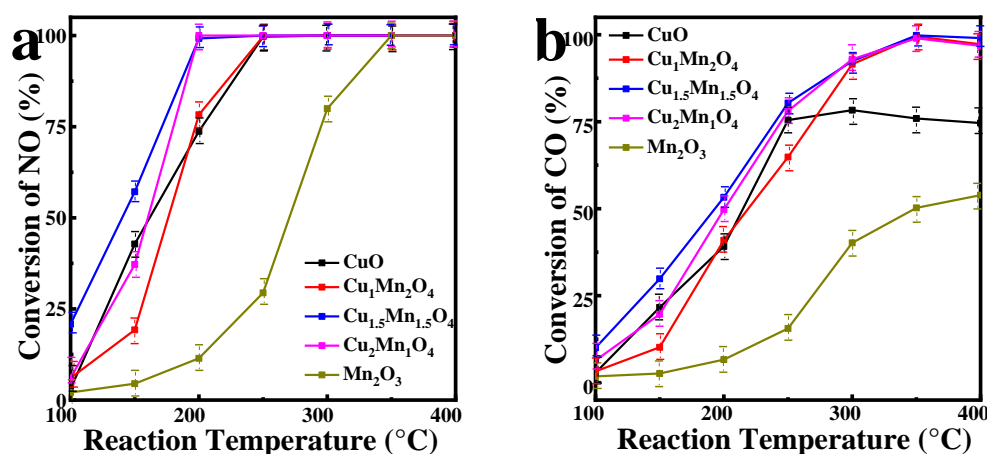


Figure 7. (a) NO conversion and (b) CO conversion of all the catalysts in the CO-SCR.

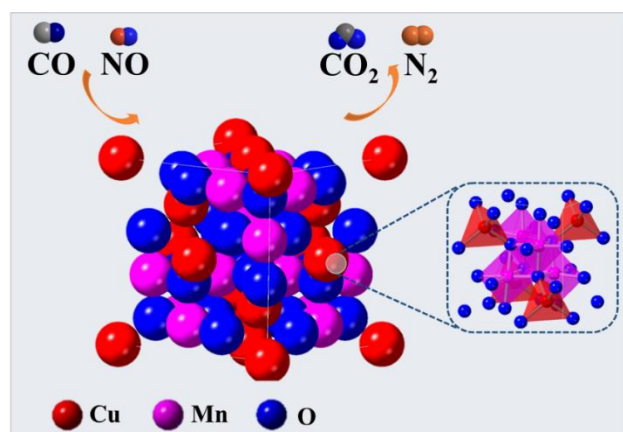
Therefore, Cu doping is conducive to the performance improvement of the Cu_xMn_{3-x}O₄ catalyst because there is a strong synergistic effect between the binary metal oxides. It is accepted that the active phase of spinel is the highly reactive center in the catalytic reaction process. The active phase of Cu_{1.5}Mn_{1.5}O₄ spinel plays an important role in the CO-SCR reaction, and the catalytic performance of the spinel structure catalyst is better than that of the other catalysts. The stability of this catalyst was further confirmed by the XRD (Figure S3a) and TEM analyses (Figure S3b,c), which showed no obvious change in the structure after the reaction at 400 °C.

3.2. Structure Activity Relationship and Catalytic Reaction Mechanism

According to reports, the active phase of Cu_xMn_{3-x}O₄ in the redox reaction is the Mn⁴⁺ concentration on the catalyst surface [30]. On Cu–Mn spinels, the number of surface-active sites and bulk concentration of Mn⁴⁺/Mn are critical to the reaction. At the same time, Cu²⁺ is transformed into Cu⁺, and Mn³⁺ is transformed into Mn⁴⁺. Mn⁴⁺ is considered to be a manganese species that has a passivation effect on the redox reaction. With the doping of copper ions in Mn₂O₃, the spinel structure with rich lattice defects and oxygen vacancies increases the concentration of Mn⁴⁺, which can adsorb reactant molecules and improve its redox performance, enhance the mobility of active oxygen species and enhance its catalytic activity. Therefore, compared with CuO and Mn₂O₃, the spinel-type copper-manganese composite oxide rich in Cu⁺ and Mn⁴⁺ will have a significantly improved activity. In

other words, due to the strong synergy between the binary metal oxides, copper doping is beneficial to the stability and catalytic performance of the $\text{Cu}_x\text{Mn}_{3-x}\text{O}_4$ catalyst.

Based on the above analysis, important information on the catalytic route was obtained, and a reasonable mechanism of the CO-SCR reaction on a $\text{Cu}_x\text{Mn}_{3-x}\text{O}_4$ catalyst was initially proposed. A proposed mechanism of the two processes is shown in Scheme 1: (i) CO and NO molecules are the first adsorbed oxygen vacancies, Mn^{4+} and Cu^{+} , on the catalyst surface. In this process, the reactant molecules CO and NO are adsorbed as CO (ads) and NO (ads). Subsequently, CO (ads) reacts with the active oxygen on the catalyst to produce CO_2 . (ii) NO molecules are adsorbed on the catalyst surface oxygen vacancy, the oxygen O of NO reacts with the oxygen vacancy, and nitrogen gas is generated. Herein, the redox cycle occurs between bimetallic oxide components ($\text{Cu}^{2+} + \text{Mn}^{3+} \rightleftharpoons \text{Cu}^{+} + \text{Mn}^{4+}$) in the $\text{Cu}_x\text{Mn}_{3-x}\text{O}_4$ spinels, and the Cu^{+} and Mn^{4+} formed by this interaction distorts the spinel structure and promotes the generation of more surface vacancies; that is, it is conducive to the activation of reactants CO and NO and forms more active species and improves the catalytic performance for CO-SCR of the catalysts.



Scheme 1. Schematic illustration of the proposed mechanism for the catalytic CO-SCR over $\text{Cu}_x\text{Mn}_{3-x}\text{O}_4$ catalysts.

4. Experimental

4.1. Material Synthesis

Specifically, $\text{Cu}_x\text{Mn}_{3-x}\text{O}_4$ ($x = 0, 1, 1.5, 2, 3$) spinels were prepared by a citrate-based modified pechini method [33–35]. $\text{Cu}(\text{NO}_3)_2 \cdot 3\text{H}_2\text{O}$ (Sinopharm Chemical Reagent Co., Ltd., Beijing, China, $\geq 99.0\%$) and $\text{Mn}(\text{NO}_3)_2$ solution (Macklin, 50% in H_2O) were dissolved in deionized water. In the calculated amount of copper nitrate trihydrate and 50% manganenitrate solution (Table 3), citric acid monohydrate (Xilong Chemical Co., Ltd., Guangzhou, China, $\geq 99.5\%$) was added at a molar ratio of 1:1 ($\text{Cu}+\text{Mn}/\text{citric acid}$). The solution was stirred for 2 h at room temperature to obtain a homogeneous mixture and then evaporated to obtain a sticky gel. The gel was dried in a 120°C oven for 6 h, forming a foam metal citrate complex. Finally, the samples were calcined in 600°C air for 8 h to form spinel oxides.

Table 3. The chemicals and their amounts used for preparing samples.

Sample	$\text{Cu}(\text{NO}_3)_2 \cdot 3\text{H}_2\text{O}$ (g)	50% $\text{Mn}(\text{NO}_3)_2$ Solution (g)	Citric Acid Monohydrate (g)
Mn_2O_3	-	23.4	11.7
$\text{Cu}_1\text{Mn}_2\text{O}_4$	5.1	15.0	11.7
$\text{Cu}_{1.5}\text{Mn}_{1.5}\text{O}_4$	7.5	11.1	11.7
$\text{Cu}_2\text{Mn}_{1.5}\text{O}_4$	9.8	7.3	11.7
CuO	15.1	-	11.7

4.2. Characterization

The powder samples were characterized by XRD with the use of a PANalytica X'Pert PRO MPD diffractometer using Cu K α radiation ($\lambda = 0.154$ nm, 40 kV, 40 mA). The crystallite sizes of all samples were calculated using the Debye–Scherrer equation. The morphology of the particles was analyzed with a JSM-7001F field-emission SEM with energy-dispersive spectroscopy (EDS) (INCA X-MAX, JEOL, Oxford, UK) and TEM (JEM-2010F, JEOL, Tokyo, Japan). The reducibility of the catalysts was examined by H₂-TPR using a Quantachrome automated chemisorption analyzer (Chem BET pulsar TPR/TPD). Briefly, 50 mg of sample was loaded into a quartz U-tube and heated from room temperature to 150 °C at 10 °C min⁻¹ under helium flow to remove moisture and impurities. Then, the sample was cooled to room temperature, followed by heating to 800 °C at a heating rate of 10 °C min⁻¹ under a binary gas mixture (10 vol.% H₂/Ar) with a gas flow rate of 30 mL min⁻¹. H₂ consumption was detected continuously as a function of increasing temperature using a thermal conductivity detector (TCD). The BETs were determined using N₂ physisorption at -196 °C using Quantachrome NOVA 3200e equipment. Prior to N₂ adsorption, each catalyst was degassed for 2 h under vacuum at 200 °C. The surface chemical composition was determined by XPS (Model VG ESCALAB 250 spectrometer, Thermo Electron, London, UK) using non-monochromatized Al K α X-ray radiation ($h\nu = 1486.6$ eV).

4.3. Measurement

The evaluation of the catalyst was carried out with a typical fixed-bed reactor with a quartz tube (8 mm inner diameter). Two grams of the catalysts (particle size was 20–40 mesh) were used in quartz tubes between glass wool. The catalytic activity was measured using feed gas compositions of 1000 ppm NO, 2000 ppm CO and N₂ (the balance) at different temperatures at a rate of 30,000 h⁻¹. First, the catalysts were treated using a CO/N₂ gas flow at 200 °C for 1 h before each test. After the catalysts were cooled to room temperature under a N₂ flow, they were allowed to react with the mixed gas. The CO, NO and NO₂ concentrations were monitored using a Testo 350 flue gas analyzer. The catalytic activity was calculated using the following formula:

$$\text{NO conversion (\%)} = \frac{\text{NO}_{\text{in}} - \text{NO}_{\text{out}}}{\text{NO}_{\text{in}}} \times 100\% \quad (1)$$

$$\text{CO conversion (\%)} = \frac{\text{CO}_{\text{in}} - \text{CO}_{\text{out}}}{\text{CO}_{\text{in}}} \times 100\% \quad (2)$$

where the “in” and “out” subscripts indicate the inlet and outlet concentrations of NO and CO in the steady state, respectively. The selectivity of N₂ was not calculated here due to no NO₂ being detected at the outlet.

5. Conclusions

In this work, a series of Cu_xMn_{3-x}O₄ spinels were synthesized by the citrate-based modified pechini method. The results show that controlling the doping amount of Cu can improve the low-temperature activity of the Mn₂O₃ catalyst. Doping Cu species could shift the redox balance in the catalyst system (Cu²⁺ + Mn³⁺ \rightleftharpoons Mn⁴⁺ + Cu⁺), improve the redox performance and catalytic activity of manganese oxide catalyst, and promote the grain formation and growth of the Cu_{1.5}Mn_{1.5}O₄ spinel structure instead of manganese oxides to increase the surface area and particle size. The surface of Cu_{1.5}Mn_{1.5}O₄ spinels retained a high ratio of Mn⁴⁺/Mn, more reactive oxygen species were formed than pure Mn₂O₃ on the surface to promote the adsorption of oxygen molecules, and it enhanced the adsorption capacity of CO and NO. In general, the doping of low valence state Cu significantly enhanced the CO–SCR activity of Cu_xMn_{3-x}O₄ spinels at low temperature, which could be an effective way to design and synthesize highly active Mn–based CO-SCR catalysts.

Supplementary Materials: The following supporting information can be downloaded at: <https://www.mdpi.com/article/10.3390/catal12060591/s1>, Figure S1: CO conversion of Cu_{1.5}Mn_{1.5}O₄ catalyst in the CO-SCR (Reaction conditions: [CO] = 2000 ppm and N₂ as balance gas, GHSV = 30,000 h⁻¹); Figure S2: (a) NO conversion; (b) N₂ selectivity in CO-SCR reaction (Reaction conditions: [NO] = 1000 ppm, [CO] = 2000 ppm, [O₂] = 0 or 1%, and N₂ as balance gas, GHSV = 30,000 h⁻¹); Figure S3: (a) XRD patterns, and (b,c) TEM images of the catalyst of Cu_{1.5}Mn_{1.5}O₄ after reaction.

Author Contributions: Conceptualization, F.F.; data curation, F.F. and L.W. (Lingjuan Wang); formal analysis, F.F., L.W. (Lingjuan Wang) and L.W. (Lei Wang); methodology, F.F. and M.W.; project administration, J.L.; writing—original draft, F.F. and M.W.; writing—review and editing, F.F., M.W. and J.L.; funding acquisition, F.F. and J.L. All authors have read and agreed to the published version of the manuscript.

Funding: This research was funded by the Chengde Science and Technology Research and Development Project (202006A117), School-level Youth Fund Project (QN2021001), the Scientific Research Project of the Higher Education Institutions of Hebei Province (ZD2021413) and the School-level teaching reform project (JG-202021571).

Data Availability Statement: Data are available from the corresponding author on request.

Conflicts of Interest: The authors declare no conflict of interest.

References

1. Liu, K.; Yu, Q.; Liu, J.; Wang, K.; Han, Z.; Xuan, Y.; Qin, Q. Selection of catalytically active elements for removing NO and CO from flue gas at low temperatures. *New J. Chem.* **2017**, *41*, 13993–13999. [[CrossRef](#)]
2. Qin, Y.; Fan, S.; Li, X.; Gan, G.; Wang, L.; Yin, Z.; Guo, X.; Tadé, M.O.; Liu, S. Peanut-shaped Cu–Mn nano-hollow spinel with oxygen vacancies as catalysts for low-temperature NO reduction by CO. *ACS Appl. Nano Mater.* **2021**, *4*, 11969–11979. [[CrossRef](#)]
3. Li, S.; Chen, X.; Wang, F.; Xie, Z.; Hao, Z.; Liu, L.; Shen, B. Promotion effect of Ni doping on the oxygen resistance property of Fe/CeO₂ catalyst for CO-SCR reaction: Activity test and mechanism investigation. *J. Hazard. Mater.* **2022**, *431*, 128622. [[CrossRef](#)] [[PubMed](#)]
4. Roy, S.; Hegde, M.; Madras, G. Catalysis for NO_x abatement. *Appl. Energy* **2009**, *86*, 2283–2297. [[CrossRef](#)]
5. Fernandez, E.; Liu, L.; Boronat, M.; Arenal, R.; Concepcion, P.; Corma, A. Low-temperature catalytic NO reduction with CO by subnanometric Pt clusters. *ACS Catal.* **2019**, *9*, 11530–11541. [[CrossRef](#)]
6. Hu, Y.; Dong, L.; Shen, M.; Liu, D.; Wang, J.; Ding, W.; Chen, Y. Influence of supports on the activities of copper oxide species in the low-temperature NO+CO reaction. *Appl. Catal. B* **2001**, *31*, 61–69. [[CrossRef](#)]
7. Ilieva, L.; Pantaleo, G.; Velinov, N.; Tabakova, T.; Petrova, P.; Ivanov, I.; Avdeev, G.; Paneva, D.; Venezia, A. NO reduction by CO over gold catalysts supported on Fe-loaded ceria. *Appl. Catal. B* **2015**, *174*, 176–184. [[CrossRef](#)]
8. Zhang, S.; Shan, J.; Zhu, Y.; Nguyen, L.; Huang, W.; Yoshida, H.; Takeda, S.; Tao, F. Restructuring transition metal oxide nanorods for 100% selectivity in reduction of nitric oxide with carbon monoxide. *Nano Lett.* **2013**, *13*, 3310–3314. [[CrossRef](#)]
9. Wang, X.; Li, X.; Mu, J.; Fan, S.; Chen, X.; Wang, L.; Yin, Z.; Tade, M.; Liu, S. Oxygen vacancy-rich porous Co₃O₄ nanosheets toward boosted NO reduction by CO and CO oxidation: Insights into the structure-activity relationship and performance enhancement mechanism. *ACS Appl. Mater. Interfaces* **2019**, *11*, 41988–41999. [[CrossRef](#)]
10. Lima, T.; Pereira, C.; Castelblanco, W.; Santos, B.; Silva, S.; Santana, R.; González, U.; Sartoratto, C. Zirconia-supported cobalt catalysts: Activity and selectivity in NO reduction by CO. *Chem. Select* **2017**, *2*, 11565–11573.
11. Salker, A.; Desai, M. Catalytic activity and mechanistic approach of NO reduction by CO over M_{0.05}Co_{2.95}O₄ (M = Rh, Pd & Ru) spinel system. *Appl. Surf. Sci.* **2016**, *389*, 344–353.
12. Liu, L.; Yao, Z.; Deng, Y.; Gao, F.; Liu, B.; Dong, L. Morphology and crystal-plane effects of nanoscale ceria on the activity of CuO/CeO₂ for NO reduction by CO. *ChemCatChem* **2011**, *3*, 978–989. [[CrossRef](#)]
13. Wang, Y.; Zhang, L.; Li, R.; He, H.; Huang, L. MOFs-based coating derived Me-ZIF-67@CuO_x materials as low-temperature NO-CO catalysts. *Chem. Eng. J.* **2019**, *381*, 122757. [[CrossRef](#)]
14. Xiaoyuan, J.; Guanghui, D.; Liping, L.; Yingxu, C.; Xiaoming, Z. Catalytic activities of CuO/TiO₂ and CuO-ZrO₂/TiO₂ in NO+CO reaction. *J. Mol. Catal. A Chem.* **2004**, *218*, 187–195. [[CrossRef](#)]
15. Boningari, T.; Pavani, S.; Ettireddy, P.; Chuang, S.; Smirniotis, P. Mechanistic investigations on NO reduction with CO over Mn/TiO₂ catalyst at low temperatures. *Mol. Catal.* **2017**, *451*, 33–42. [[CrossRef](#)]
16. Shan, J.; Zhu, Y.; Zhang, S.; Zhu, T.; Rouvimov, S.; Tao, F. Catalytic Performance and in Situ Surface Chemistry of Pure α-MnO₂ Nanorods in Selective Reduction of NO and N₂O with CO. *J. Phys. Chem. C* **2013**, *117*, 8329–8335. [[CrossRef](#)]
17. Deng, C.; Li, B.; Dong, L.; Zhang, F.; Fan, M.; Jin, G.; Gao, J.; Gao, L.; Zhang, F. NO reduction by CO over CuO supported on CeO₂-doped TiO₂: The effect of the amount of a few CeO₂. *Phys. Chem.* **2015**, *17*, 16092–16109. [[CrossRef](#)]
18. Li, Y.; Wan, Y.; Li, Y.; Zhan, S.; Guan, Q.; Tian, Y. Low-temperature selective catalytic reduction of NO with NH₃ over Mn₂O₃-Doped Fe₂O₃ hexagonal microsheets. *ACS Appl. Mater. Interfaces* **2016**, *8*, 5224–5233. [[CrossRef](#)]

19. Liu, J.; Wei, Y.; Li, P.; Zhang, P.; Su, W.; Sun, Y.; Zou, R.; Zhao, Y. Experimental and theoretical investigation of mesoporous MnO₂ nanosheets with oxygen vacancies for high-efficiency catalytic deNO_x. *ACS Catal.* **2018**, *8*, 3865–3874. [[CrossRef](#)]
20. Pan, K.; Young, C.; Pan, G.; Chang, M. Catalytic reduction of NO by CO with Cu-based and Mn-based catalysts. *Catal. Today* **2020**, *348*, 15–25. [[CrossRef](#)]
21. Yao, X.; Xiong, Y.; Sun, J.; Gao, F.; Deng, Y.; Tang, C.; Dong, L. Influence of MnO₂ modification methods on the catalytic performance of CuO/CeO₂ for NO reduction by CO. *J. Rare Earths* **2014**, *32*, 131–138. [[CrossRef](#)]
22. Li, D.; Yu, Q.; Li, S.; Wan, H.; Liu, L.; Qi, J.; Liu, L.; Gao, F.; Dong, L.; Chen, Y. The remarkable enhancement of CO-pretreated CuO-Mn₂O₃/γ-Al₂O₃ supported catalyst for the reduction of NO with CO: The formation of surface synergetic oxygen vacancy. *Chem. A Eur. J.* **2011**, *17*, 5668–5679. [[CrossRef](#)] [[PubMed](#)]
23. Wang, X.; Lu, Y.; Tan, W.; Liu, A.; Ji, J.; Wan, H.; Sun, C.; Tang, C.; Dong, L. Insights into the precursor effect on the surface structure of γ-Al₂O₃ and NO+CO catalytic performance of CO-pretreated CuO/MnO_x/γ-Al₂O₃ catalysts. *J. Colloid Interface Sci.* **2019**, *554*, 611–618. [[CrossRef](#)] [[PubMed](#)]
24. Spassova, I.; Khristova, M.; Panayotov, D.; Mehandjiev, D. Coprecipitated CuO-MnO_x vatalysts for low-temperature CO-NO and CO-NO-O₂ reactions. *J. Catal.* **1999**, *185*, 43–57. [[CrossRef](#)]
25. Li, L.; Wang, Y.; Zhang, L.; Yu, Y.; He, H. Low-temperature selective catalytic reduction of NO_x on MnO₂ octahedral molecular sieves (OMS-2) doped with Co. *Catalysts* **2020**, *10*, 396. [[CrossRef](#)]
26. Shi, Y.; Chu, Q.; Xiong, W.; Gao, J.; Ding, Y. A new type bimetallic NiMn-MOF-74 as an efficient low-temperatures catalyst for selective catalytic reduction of NO by CO. *Chem. Eng. Process.* **2020**, *159*, 108232. [[CrossRef](#)]
27. Yi, Y.; Liu, H.; Chu, B.; Qin, Z.; Dong, L.; He, H.; Tang, C.; Fan, M.; Bin, L. Catalytic removal NO by CO over LaNi_{0.5}M_{0.5}O₃ (M = Co, Mn, Cu) perovskite oxide catalysts: Tune surface chemical composition to improve N₂ selectivity. *Chem. Eng. J.* **2019**, *369*, 511–521. [[CrossRef](#)]
28. Shi, X.; Chu, B.; Wang, F.; Wei, X.; Teng, L.; Fan, M.; Li, B.; Dong, L. Mn-Modified CuO, CuFe₂O₄, and γ-Fe₂O₃ Three-phase strong synergistic coexistence catalyst system for NO reduction by CO with a wider active window. *ACS Appl. Mater. Interfaces* **2018**, *10*, 40509–40522. [[CrossRef](#)]
29. Wan, H.; Li, D.; Dai, Y.; Hu, Y.; Liu, B.; Dong, L. Catalytic behaviors of CuO supported on Mn₂O₃ modified γ-Al₂O₃ for NO reduction by CO. *J. Mol. Catal. A Chem.* **2010**, *332*, 32–44. [[CrossRef](#)]
30. Liu, T.; Yao, Y.; Wei, L.; Shi, Z.; Han, L.; Yuan, H.; Li, B.; Dong, L.; Wang, F.; Sun, C. Preparation and evaluation of copper-manganese oxide as a high-efficiency catalyst for CO oxidation and NO reduction by CO. *J. Phys. Chem. C.* **2017**, *121*, 12757–12770. [[CrossRef](#)]
31. Li, J.; Zhang, W.; Li, C.; He, C. Efficient catalytic degradation of toluene at a readily prepared Mn-Cu catalyst: Catalytic performance and reaction pathway. *J. Colloid Interface Sci.* **2021**, *591*, 396–408. [[CrossRef](#)] [[PubMed](#)]
32. Zhang, L.; Shi, L.; Huang, L.; Zhang, J.; Gao, R.; Zhang, D. Rational design of high-performance seNO_x catalysts based on Mn_xCo_{3-x}O₄ nanocages derived from metal-organic frameworks. *ACS Catal.* **2014**, *4*, 1753–1763. [[CrossRef](#)]
33. Salker, A.V.; Desai, M. CO-NO/O₂ redox reactions over Cu substituted cobalt oxide spinels. *Catal. Commun.* **2016**, *87*, 116–119. [[CrossRef](#)]
34. Salker, A.; Desai, M. Low-temperature nitric oxide reduction over silver-substituted cobalt oxide spinels. *Catal. Sci. Technol.* **2016**, *6*, 430–433. [[CrossRef](#)]
35. Liu, S.; Ji, Y.; Xu, W.; Zhang, J.; Jiang, R.; Li, L.; Jia, L.; Zhong, Z.; Xu, G.; Zhu, T.; et al. Hierarchically interconnected porous Mn_xCo_{3-x}O₄ spinels for low-temperature catalytic reduction of NO by CO. *J. Catal.* **2022**, *406*, 72–86. [[CrossRef](#)]